



**HAL**  
open science

## Ionic liquid redox flow membraneless battery in microfluidic system

Nesrine Chaabene, Kieu Ngo, Mireille Turmine, Vincent Vivier

### ► To cite this version:

Nesrine Chaabene, Kieu Ngo, Mireille Turmine, Vincent Vivier. Ionic liquid redox flow membraneless battery in microfluidic system. *Journal of Energy Storage*, 2023, 57, pp.106270. 10.1016/j.est.2022.106270 . hal-04775517

**HAL Id: hal-04775517**

**<https://hal.science/hal-04775517v1>**

Submitted on 10 Nov 2024

**HAL** is a multi-disciplinary open access archive for the deposit and dissemination of scientific research documents, whether they are published or not. The documents may come from teaching and research institutions in France or abroad, or from public or private research centers.

L'archive ouverte pluridisciplinaire **HAL**, est destinée au dépôt et à la diffusion de documents scientifiques de niveau recherche, publiés ou non, émanant des établissements d'enseignement et de recherche français ou étrangers, des laboratoires publics ou privés.

# 1 Ionic liquid redox flow membraneless battery in microfluidic system

2 Nesrine CHAABENE,<sup>1</sup> Kieu NGO,<sup>1,§,\*</sup> Mireille TURMINE,<sup>1,§</sup> Vincent VIVIER<sup>1,§</sup>

3 <sup>1</sup>. *Sorbonne Université, CNRS, Laboratoire Interfaces et Systèmes Electrochimiques,*

4 *LISE, F-75005 Paris, France*

## 5 Abstract

6 Redox flow batteries (RFBs) often require the presence of a physical membrane to  
7 separate the two compartments of the battery. The objective of this work is to develop a  
8 membraneless microfluidic redox flow battery (RFB) by using 1-ethyl-3-methylimidazolium  
9 bis(trifluoromethylsulfonyl)imide (C<sub>2</sub>mimTFSI) as support electrolyte in which Quinone (Q)  
10 and iron chloride (FeCl<sub>2</sub>) have been used as negolyte (or anolyte) and posolyte (or catholyte),  
11 respectively. Polarization curve and cyclic voltammetry were used to characterize the  
12 electrochemical properties of the electrochemical systems as well as the performance of the  
13 microbattery. The proof-of-concept of the system is presented with an open circuit potential of  
14 0.6 V, obtained with both polarization curve and cyclic voltammetry, and with a current density  
15 ranging from 0.3 to 0.65 mA.cm<sup>-2</sup> for total flow rates of 10 to 20 μL.min<sup>-1</sup>. A maximum power  
16 of 40 μWcm<sup>-2</sup> has been obtained with this microbattery.

17  
18 **Keywords:** C<sub>2</sub>mimTFSI, Quinone, FeCl<sub>2</sub>, redox flow batteries, membraneless electrochemical  
19 cell, microfluidics

---

\* Corresponding author: Kieu Ngo ([kieu.ngo@sorbonne-universite.fr](mailto:kieu.ngo@sorbonne-universite.fr))

§ present address: *Sorbonne Université, CNRS, Laboratoire Réactivité de Surface, LRS UMR7197, F-75005 Paris, France*

## 21 **1. Introduction**

22           The development of environmentally friendly devices for the storage of renewable  
23 energy has become a subject of paramount importance. For instance, the use of less volatile and  
24 less toxic chemicals such as ionic liquids (ILs) for a “green chemistry” is a trend that aims to  
25 reduce global pollution. These molten salts at room temperature are characterized by their  
26 thermal and electrochemical stabilities, a low melting point in comparison with conventional  
27 salts (*i.e.*, below 100 °C), a low vapor pressure and wide electrochemical potential windows.  
28 Therefore, they have been progressively receiving a lot of interest in various electrochemical  
29 applications including electrodeposition, electroplating, electropolishing, and electrolyte for  
30 redox flow batteries (RFBs) [1-3].

31           These latter provide direct conversion between chemical and electrical energy and have  
32 been widely used as one of the most robust storage systems for renewable energy due to their  
33 relatively simple installation and fast response time as well as their wide range of power and  
34 energy, suitable for a variety of practical applications. The main advantage of RFBs is their  
35 ability to decouple power and energy of the system. In fact, the energy storage capacity depends  
36 on both the concentration of the electroactive species dissolved in the electrolyte and the volume  
37 of the storage tanks, while the power of the system depends on the number of individual cells  
38 and the electroactive surface of the electrodes. These features render RFBs unique, compared  
39 to other energy storage systems such as lithium-based batteries, allowing greater flexibility in  
40 the individual optimization of power or energy depending on the target application. Despite the  
41 fact that almost all aspect RFBs have been studied and that all-vanadium RFBs have been  
42 commercialized for various applications including for grid storage, some factors limiting their  
43 industrialization on wider scale still exist [4-6]. In particular, many studies have highlighted the  
44 need for optimization of the separating membrane, which is a key component of RFB [7-9]. For  
45 example, if one thinks solely in terms of cost, the separator membrane alone accounts for more

46 than 10% of the total cost for the vanadium RFBs [10]. In addition, the separator membrane  
47 must ensure high proton conductivity, whereas at the same time, the main current issues  
48 associated with the use of membrane are numerous, including posolyte and negolyte crossover  
49 through the separator, ohmic losses and the swelling and shrinking of the membrane due to the  
50 water uptake.

51 Among the various membrane optimization strategies to improve cell performance,  
52 membraneless redox flow batteries in microfluidic-based devices are a promising alternative.  
53 In these systems, the membrane separator in classical RFBs is eliminated avoiding or improving  
54 the aforementioned issues. Since for microfluidic devices, the characteristic dimension of  
55 channels is in the order of a hundred of micrometers, it is then relatively simple to achieve a  
56 low Reynolds number, resulting in the establishment of co-laminar flows. Therefore, this  
57 confined liquid/liquid interface in the microchannel can be considered as a virtual membrane  
58 playing the same role than a physical separator membrane. Thanks to the co-laminar regime,  
59 the two streams (posolyte and negolyte) containing different electroactive species at different  
60 concentrations do not convectively interpenetrate and flow side by side in the microchannel  
61 [11-15].

62 The concept of membraneless redox-flow batteries was first reported by Ferrigno *et al.* [16]  
63 in 2002, with the development of a millimeter-scale redox fuel cell. The two streams contained  
64 the redox couples  $V^{5+}/V^{4+}$  and  $V^{3+}/V^{2+}$  in 25%  $H_2SO_4$  as posolyte and negolyte, respectively.  
65 Carbon-on-gold electrodes were used as current collectors rather than metals to reduce the  
66 electrolysis of water as side reactions. This membraneless RFB shows an open circuit voltage  
67 of 1.59 V and a maximum current density of 80 mA.cm<sup>-2</sup>. More recently, Navalpotro *et al.* [17]  
68 reported a membraneless redox flow battery in which vanadium species were replaced by  
69 quinone; the two streams being formed by an acidic aqueous solution of hydroquinone ( $H_2Q$ )  
70 and 1-butyl-1-methylpyrrolidinium bis(trifluoromethanesulfonyl)imide ( $PYR_{14}TFSI$ )

71 containing dissolved parabenzoquinone (pBQ) paving the way to the use of ionic liquids in  
72 these batteries. However, in this study, the authors played on the immiscibility of the two  
73 electrolytes in such a way as to exclude membrane use. The open circuit voltage and energy  
74 density were shown to be 1.4 V and 22.5 WhL<sup>-1</sup>, respectively. By using different immiscible  
75 electrolytes [18] or by changing the redox couple involved in the electrochemical systems [19]  
76 both larger operating voltage and power density could have been reached [20]. Interestingly,  
77 aqueous membrane-free batteries involving aqueous/aqueous immiscible electrolytes were also  
78 investigated showing that in this case, the partition of the electroactive species is a key  
79 parameter for these systems working as aqueous biphasic systems (ABS) [21]. However, a large  
80 scale membraneless RFB remains a challenge since the mixing of electrolytes is difficult to  
81 avoid under dynamic flow conditions [22], whereas the miniaturization of the battery will  
82 naturally result in a laminar flow.

83 To the best of our knowledge, and despite the fact that the use of ionic liquids and deep  
84 eutectic solvents as electrolytes in RFBs as well as the development of micro-electromechanical  
85 systems MEMS-based membraneless RFB have been described in the literature [23-25], the  
86 combination of these two components, which should lead to development of high power and  
87 membraneless microbatteries, has not yet been reported. In fact, the use of ionic liquids and  
88 deep eutectic solvents is beneficial as it allows to obtain a wide electrochemical window as well  
89 as a laminar flow in the microchannel thank to their relatively high viscosity compared to the  
90 usual electrolytes utilized in RFB. This laminar regime allows to eliminate the separating  
91 membrane of the battery.

92 The objective of this work is to develop a membraneless RFB by using 1-ethyl-3-  
93 methylimidazolium (bistrifluoromethylsulfonyl)imide (C<sub>2</sub>mimTFSI) as support electrolyte and  
94 Quinone (Q) and iron chloride (FeCl<sub>2</sub>) as electroactive species in a microfluidic system. This  
95 IL was selected because of its low viscosity and high conductivity compared to other ILs.

106 Moreover, C<sub>2</sub>mimTFSI has a large electrochemical window which seems to be suitable for this  
107 application [26]. We first report on the physicochemical properties such as viscosity and  
108 electrochemical potential window of the synthesized C<sub>2</sub>mimTFSI as well as its electrochemical  
109 properties with the two redox mediators. Finally, the proof-of-concept of this new system will  
110 be shown with the use of a simple microfluidic device.

101

## 102 **2. Experimental section**

### 103 ***2.1. Electrolyte preparation and electrochemical characterizations***

104 The electrolyte consisted of C<sub>2</sub>mimTFSI, which was prepared according to the  
105 experimental procedure previously described [27], and whose chemical structure is shown in  
106 Table 1. The viscosity of the ionic liquid was measured with a rolling-ball viscosimeter (Anton  
107 Paar, Lovis 2000M/ME). The ionic conductivity was measured using a Lab CDM 230  
108 conductimeter (Radiometer Analytical). The variations in viscosity were studied over a  
109 temperature range between 20 to 60°C. The electroactive species quinone (purity ≥ 98%) and  
110 iron chloride, FeCl<sub>2</sub> (98%) were supplied by Sigma-Aldrich and used as received.

111 The electrochemical characterization of the negolyte and posolyte was performed in a  
112 three-electrode cell configuration using a GAMRY REF 600 potentiostat. A gold electrode of  
113 100 μm in radius ( $S = 3.14 \cdot 10^{-4} \text{ cm}^2$ ) was used as the working electrode, a platinum gauze of 1  
114 cm<sup>2</sup> surface area as the counter electrode, and a home-made reference electrode based on Ag/  
115 AgNO<sub>3</sub> saturated in IL. However, all the potentials will be reported with respect to the  
116 ferrocenemethanol couple (Fc<sup>+</sup>MeOH/FcMeOH) which was used as internal standard for  
117 electrochemical measurements.

118

119

## 120 **2.2. Microfluidic device fabrication and characterization**

121 The microfluidic cell was a Y-type channel and a pair of gold microelectrodes was used  
122 as current collectors as sketched in Fig. 1. The millimeter-scale device consists of a main  
123 channel (length 30 mm, width 3mm and height 0.5 mm) connected to two inlets and two outlets  
124 for handling the electrolytes. The cell in PDMS and gold microelectrodes were fabricated using  
125 classical soft lithography and lift-off process. All the details about the device fabrication can be  
126 found in previous work [28]. Briefly, microelectrodes consisting of a gold layer of 200 nm and  
127 a thin adhesion layer of Cr (10 nm) were deposited in a glass substrate using PECVD process.  
128 Microfluidic channel was fabricated by using the conventional molding technique of PDMS,  
129 using molds printed either by 3D printer or photolithography fabrication. The gold electrodes  
130 were positioned in the middle of the channel with a spacing of 0.5 mm leading to an active  
131 electrode area of 0.025 cm<sup>2</sup>. Finally, the channel was covalently bonded to the glass substrate  
132 by treating both the PDMS surface and the glass substrate with an oxygen plasma. The precise  
133 positioning was performed with the help of marks which were added on the glass substrate, to  
134 manually align the microfluidic channel and the electrodes.

135 The supporting electrolytes (C<sub>2</sub>mimTFSI) containing the redox mediators were injected  
136 into the channel by using a pressure controller (Fluigent MFCS-EZ) offering a precise control  
137 of the flow-rates. All experiments were performed using an inverted microscope (Zeiss  
138 Axiovert 40 CFL) for observing the laminar flow in the channel. To determine the cell  
139 performance, a polarization curve was recorded using a high input impedance voltmeter  
140 (Solartron 7055) and pure resistors of different values.

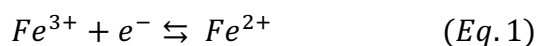
141

## 142 **3. Results and discussion**

### 143 **3.1. Electrochemical characterization of the electroactive species in C<sub>2</sub>mimTFSI**

144 Table 1 shows three pictures corresponding to the pure ionic liquid (C<sub>2</sub>mimTFSI),  
 145 quinone (0.35M) in C<sub>2</sub>mimTFSI and FeCl<sub>2</sub> (0.1 M) in C<sub>2</sub>mimTFSI, respectively. It is worth  
 146 noting that these given concentrations represent the maximum concentrations that can be  
 147 soluble in the used ionic liquid. All experiments in this work have been performed with these  
 148 concentrations. Fig. 2 shows the electrochemical characterization of C<sub>2</sub>mimTFSI as electrolyte  
 149 in the presence and in the absence of the electroactive species using a gold electrode of 100 μm  
 150 in radius. The electrochemical potential window of the ionic liquid was determined using linear  
 151 sweep voltammetry (LSV, scan rate 5 mVs<sup>-1</sup>). As shown in Fig. 2a (black curve), the  
 152 electrochemical window of C<sub>2</sub>mimTFSI is about 3.5 V which is in agreement with other study  
 153 on this ionic liquid [17]. It is noteworthy that this value is much higher than that of aqueous  
 154 electrolyte [23] thus enlarging the choice of redox couples to two electrochemical systems with  
 155 a higher standard potential difference, thus resulting in higher open circuit potential for the  
 156 electrochemical cell.

157 Fig. 2a also shows cyclic voltammograms (CVs) of ferrous ions (0.1 M) in C<sub>2</sub>mimTFSI  
 158 using gold electrode recorded as a function of the scan rates from 50 mVs<sup>-1</sup> to 1 Vs<sup>-1</sup>. Two  
 159 well-defined peaks centered at -0.1 V vs Fc<sup>+</sup>/Fc can be seen and correspond to the one electron  
 160 exchange:



163  
 164 The analysis of CV curves allows the determination of Faradaic peak current,  $I_p$ , and  
 165 peak potential,  $E_p$ , as a function of the scan rate,  $v$ . When the scan rate is low enough, the  
 166 electrochemical system is reversible and the peak intensity is given by [29]:

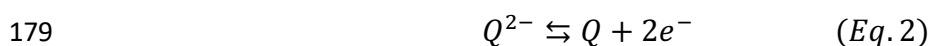
$$167 \quad I_p = 0.446n^{3/2}FSC^0\sqrt{D}\sqrt{\frac{Fv}{RT}}$$



168 where  $n$  is the number of electrons,  $F$  is the Faraday constant,  $S$  the electrode surface area,  $C^0$   
169 the bulk concentration of the electroactive species,  $R$  the gas constant,  $D$  the diffusion  
170 coefficient, and  $T$  the absolute temperature (in K).

171 An important feature for a reversible system is the independence of the peak potential  
172 as a function of the scan rate. Additionally, the peak width,  $E_{p/2} - E_p$ , is 56.5 mV and the  
173 anodic to cathodic peak potential difference is 57 mV (at 25°C). The slope of the  $I_p = f(\sqrt{v})$   
174 curve is  $2.79 \mu\text{As}^{1/2}\text{V}^{-1/2}\text{cm}^{-2}$ , leading to a diffusion coefficient of about  $(1.1 \pm$   
175  $0.1) 10^{-8} \text{ cm}^2 \text{ s}^{-1}$ .

176 Cyclic voltammograms of quinone (0.35 M) in  $\text{C}_2\text{mimTFSI}$  as a function of the scan  
177 rates are shown in Fig. 3. The two observed peaks refer to the redox reactions of quinone  
178 according to Eq. 2:



180  
181 Similarly, the current density increases with the scan rates while the oxidation peak  
182 increases more quickly than the reduction peak. In addition, the difference between the anodic  
183 and cathodic peak potentials is 695 mV at  $50 \text{ mVs}^{-1}$  and increases to 784 mV at  $1000 \text{ mVs}^{-1}$   
184 which confirms that this system behaves as a quasi-reversible redox couple in this media. This  
185 behavior is contrary to the results in aqueous medium [26] in which a series of organic  
186 molecules based on quinone exhibit a reversible kinetics in the same scan rate range.

187  
188 In order to determine the open circuit potential expected in a redox cell, cyclic  
189 voltammograms of both  $\text{FeCl}_2$  (0.1 M) and quinone (0.35 M) at  $50 \text{ mVs}^{-1}$  are plotted in Fig. 4.  
190 A potential difference of 0.64 V is observed.

191

192 **3.2. Performances of membraneless IL-based RFB**

193 **3.2.1. Laminar flow and open circuit potential**

194 The viscosity of the negolyte and posolyte is a key factor in a membraneless RFB since  
195 it has a genuine effect in various properties such as the ability to generate co-laminar flows in  
196 microchannel, the mass transport rates inside the electrolyte and the required pumping power  
197 to ensure a good operation of the RFB. Thus, the viscosity of pure C<sub>2</sub>mimTFSI, and of the  
198 solutions containing each electroactive species in the IL were measured as a function of  
199 temperature ranging from 20 to 60 °C (Fig. 5).

200 At room temperature, the value of the dynamic viscosity of pure C<sub>2</sub>mimTFSI is equal  
201 to 30.4 mPa.s which is close to the value reported in the literature [30]. As shown in Fig. 5, the  
202 viscosities of the three solutions decrease when the temperature increases. Moreover, it is  
203 important to note that the addition of electroactive species does not significantly change the  
204 viscosity of the electrolyte (less than 5%). This value should be compared to that of pure water  
205 at room temperature, 0.9 mPa.s, and that of concentrated sulfuric acid solutions usually used in  
206 all vanadium redox flow battery, between 4 and 6 mPa.s, showing that the viscosity value of  
207 the ionic liquid is indeed thirty times higher than that of water but only six times that of sulfuric  
208 acid usually used in these applications.

209 In order to characterize the flow in the channel, the Reynolds number ( $R_e$ ) was  
210 calculated as

211

212 
$$R_e = \frac{\rho v d}{\eta} = \frac{1513.6 * 1.66 * 10^{-4} * 0.5 * 10^{-3}}{31.32 * 10^{-3}} = 0.004$$

213

214 where  $\rho$  is the density of the fluid ( $\text{kg/m}^3$ ),  $v$  is the flow speed ( $\text{m/s}$ ),  $d$  is the characteristic  
215 dimension of the channel ( $\text{m}$ ),  $\eta$  is the dynamic viscosity of the fluid ( $\text{Pa}\cdot\text{s}$ ). The obtained value  
216 of 0.004 corresponds to a laminar flow in the microfluidic channel.

217 It is interesting to note that the solutions used in this study are differently colored. Thus,  
218 the negolyte is dark blue and the posolyte is yellow (as can be seen in Table 1 from the color of  
219 the chemicals), which allows a direct visualization of the co-laminar flow in the microchannel  
220 and verifying that no interdiffusion of the species occurs during flow. Additionally, in order to  
221 check that a co-laminar flow has been well established in the microchannel (Fig. 6a), flow rate  
222 ratios of negolyte/posolyte streams can be varied by maintaining the total flow rate constant at  
223 a value of  $30 \mu\text{L min}^{-1}$ . Images of the circulating fluids as well as the measured open circuit  
224 potentials are presented in Table 2. Interestingly, the confined liquid/liquid interface between  
225 the two streams moves when the flow rates ratio change without any apparent mixing. In  
226 particular, a symmetrical flow regime is established between the streams when the same flow  
227 rate is applied for each negolyte and posolyte streams (flow rate of  $15 \mu\text{L min}^{-1}$ ). In addition, a  
228 zero open circuit potential ( $E_{oc}$ ) is measured when there is only one electrolyte (negolyte or  
229 posolyte) in the main channel (i.e., for flow rates of 30/0 or 0/30, respectively). Then, this open  
230 circuit potential value varies as a function of the flow rates to reach an expected value of 0.61  
231 V when the flow rate of the two streams is of the same order of magnitude. In conclusion,  
232 whatever the flow rate ratios between the two streams, a co-laminar regime is well established  
233 in the microfluidic redox-flow battery.

234

### 235 3.2.2. Polarization curves

236 The experimental set-up of the membraneless RFB shown on Fig. 6a was used to address  
237 the polarization curves of the cell, which is the most used technique to characterize the  
238 performance of a battery. In order to study the influence of the total flow rate in the main

239 channel on the performance of the cell, two total flow rates of 10 and 20  $\mu\text{L min}^{-1}$ , with the  
240 same flow rate ratio between negolyte and posolyte streams, were used. The corresponding  
241 polarization curves of the cell are shown in Fig. 6b and 6c, respectively.

242 The maximum value of the open circuit potential is about 0.64 V for a total flow rate of  
243 10  $\mu\text{L}\cdot\text{min}^{-1}$  (Fig. 6b); this open circuit potential value perfectly agrees with that obtained by  
244 cyclic voltammetry and corresponds to thermodynamic value. Two distinct voltage loss regimes  
245 can be clearly observed: at low current density, the potential linearly decreases when the current  
246 density increases which corresponds to the activation losses and then the ohmic loss regime. It  
247 is noteworthy that for both flow rates, no mass transfer region is observed as expected in the  
248 polarization curves [31]. This phenomenon can be ascribed to the electrodes geometry, as well  
249 described in the literature [32].

250 The maximum power of this battery is obtained for the higher total flow rate (20  $\mu\text{L}$   
251  $\text{min}^{-1}$ , Fig. 6c) with a power of 40  $\mu\text{W cm}^{-2}$  for a current density of 0.3  $\text{mA cm}^{-2}$ . The power is  
252 higher for 20  $\mu\text{L min}^{-1}$  since this flow rate allows a faster replenishment of the depletion layer  
253 on planar electrodes than for lower flow rate. Nevertheless, the value of the power remains low  
254 due to the fact that the reaction occurs at a planar electrode [32-33]. These results show the  
255 possibility of working in a cell without membrane, the use of ionic liquids being beneficial to  
256 maintain an interface between two liquids, but also offering the possibility to use other redox  
257 couples than vanadium.

258

#### 259 **4. Conclusion**

260 In this work, we showed that the combination of ionic liquids and microfluidics is  
261 promising for the development of a membraneless redox-flow microdevice. Thanks to the  
262 viscosity of  $\text{C}_2\text{mimTFSI}$  and the millimeter-scale of the cell, co-laminar flows were obtained  
263 and well controlled at the interface between negolyte and posolyte streams for different flow

264 rate ratios. The proof-of-concept of a membraneless ionic liquid-based redox flow battery has  
265 been demonstrated with an open circuit potential of 0.64 V and with a density current ranging  
266 from 0.3 to 0.65 mA cm<sup>-2</sup> for total flow rates of 10 to 20 μL min<sup>-1</sup> and a maximum of power of  
267 40 μW.cm<sup>-2</sup>.

268 The low performance of this system compared to others RFBs can be explained by the  
269 geometry of the planar electrodes, leading to significant diffusion limitations, and by the low  
270 solubility of the electroactive species in ionic liquid. Different strategies can help to enhance  
271 the performance of the cell including, for example, the mixture of this ionic liquid with a  
272 molecular solvent to increase the electrolyte solubility and the use of 3D porous carbon  
273 electrodes due to their large surface area.

274

275 **1. Acknowledgements**

276 This work was supported by the Ecole Doctorale Chimie Physique et Chimie Analytique de  
277 Paris Centre (ED 388) at Sorbonne Université.

278 **References**

- 279 1. Abbott, A.P. and McKenzie, K.J., *Application of ionic liquids to the electrodeposition of*  
280 *metals*. *Physical Chemistry Chemical Physics*, 2006. **8**(37): p. 4265-4279.
- 281
- 282 2. Loftis, J.D. and Abdel-Fattah, T.M., *Nanoscale electropolishing of high-purity nickel with*  
283 *an ionic liquid*. *International Journal of Minerals, Metallurgy, and Materials*, 2019.  
284 **26**(5): p. 649-656.
- 285
- 286 3. Lewandowski, A. and Świdorska-Mocek, A., *Ionic liquids as electrolytes for Li-ion*  
287 *batteries—an overview of electrochemical studies*. *Journal of Power sources*, 2009.  
288 **194**(2): p. 601-609.
- 289
- 290 4. Sloveichik, G. L., *Flow batteries: current status and trends*, *Chem. Rev.*, 2015, **115** (20):  
291 p. 11533-11558.
- 292 5. Kear, G., et al., *Development of the all-vanadium redox flow battery for energy storage:*  
293 *a review of technological, financial and policy aspects*, *Int. J. Energy Res.* 2012, **36**: p.  
294 1105-1120.
- 295 6. Weber, A. Z., et al., *Redox flow batteries: a review*, *Journal of Applied Electrochemistry*,  
296 2011, **41**: p. 1137-1164.
- 297 7. Möegelin, H., et al., *Effect of the pore size and surface modification of porous glass*  
298 *membranes on vanadium redox-flow battery performance*, *Journal of Applied*  
299 *Electrochemistry*, 2018, **48**: p. 651-662.
- 300 8. Lehmann, M. L., et al., *Membrane design for non-aqueous redox flow batteries: Current*  
301 *status and path forward*, *Chem*, 2022, **8** (9): p. 1611-1636.
- 302 9. Machado, C. A., et al., *Redox flow battery: improving battery performance by*  
303 *leveraging structure-property relationships*, *ACS Energy Lett.* 2021, **6**(1): p. 158-176.

- 304 10. Darling, R.M., et al., *Pathways to low-cost electrochemical energy storage: a*  
305 *comparison of aqueous and nonaqueous flow batteries*. Energy & Environmental  
306 Science, 2014. **7**(11): p. 3459-3477.
- 307
- 308 11. Bamgbopa, M. O., et al. *Prospects of recently developed membraneless cell designs for*  
309 *redox flow batteries*, Renewable and Sustainable Energy Reviews, 2017, **70**: p. 506-  
310 518.
- 311
- 312 12. Molina-Osorio, A. F., et al., *Membraneless energy conversion and storage using*  
313 *immiscible electrolyte solutions*, Current Opinion in Electrochemistry, 2020, **21**: p. 100-  
314 108.
- 315
- 316 13. Wang, X., et al., *A membrane-free, aqueous/nonaqueous hybrid redox flow battery*,  
317 Energy storage materials, 2022, **45**: p. 1100-1108.
- 318
- 319 14. Goulet, M. A., et al., *Co-laminar flow cells for electrochemical energy conversion*,  
320 Journal of Power Sources, 2014, **260**: p. 186-196.
- 321
- 322 15. Park, H. B., et al., *Performance of H-shaped membraneless micro fuel cells*, Journal of  
323 Power Sources, 2013, **226**: p. 266-271.
- 324
- 325 16. Ferrigno, R., et al., *Membraneless vanadium redox fuel cell using laminar flow*, Journal  
326 of the American Chemical Society, 2002. **124**(44): p. 12930-12931.
- 327
- 328 17. Navalpotro, P., et al., *A Membrane-Free Redox Flow Battery with Two Immiscible Redox*  
329 *Electrolytes*. Angewandte Chemie-International Edition, 2017. **56**(41): p. 12460.
- 330
- 331 18. Navalpotro, P., et al., *Exploring the versatility of membrane-free battery concept using*  
332 *different combinations of immiscible redox electrolytes*, ACS Appl. Mater. Interfaces,  
333 2018, **10**: p. 41246–41256.

334

- 335 19. Bamgbopa, M. O., et al., *Cyclable membraneless redox flow batteries based on*  
336 *immiscible liquid electrolytes: demonstration with all-iron redox chemistry*,  
337 *Electrochim. Acta.*, 2018, **267**: p. 41–50.
- 338
- 339 20. Sanchez-Díez, E., et al., *Redox flow batteries: Status and perspective towards*  
340 *sustainable stationary energy storage*, *Journal of Power Sources*, 2021, **481**: p. 228804.
- 341
- 342 21. Navalpotro, P., et al., *Critical aspects of membrane-free aqueous battery based on two*  
343 *immiscible neutral electrolytes*, *Energy Storage Materials*, 2020, **26**: p. 400-407.
- 344
- 345 22. Joseph, A., et al., *Ionic liquid and ionanofluid-based redox flow batteries – A mini*  
346 *review*, *Energies* 2022, **15**(13) : p. 4545.
- 347
- 348 23. Chakrabarti, M.H., et al., *Prospects of applying ionic liquids and deep eutectic solvents*  
349 *for renewable energy storage by means of redox flow batteries*. *Renewable and*  
350 *Sustainable Energy Reviews*, 2014. **30**: p. 254-270.
- 351
- 352 24. Shaegh, S.A.M., N.-T. Nguyen, and S.H. Chan, *A review on membraneless laminar flow-*  
353 *based fuel cells*. *International Journal of Hydrogen Energy*, 2011. **36**(9): p. 5675-5694.
- 354
- 355 25. Ejigu, A., P.A. Greatorex-Davies, and D.A. Walsh, *Room temperature ionic liquid*  
356 *electrolytes for redox flow batteries*. *Electrochemistry communications*, 2015. **54**: p.  
357 55-59.
- 358
- 359 26. Khalil, R., et al., *Effect of the chain lengthening on transport properties of imidazolium-*  
360 *based ionic liquids*. *Fluid Phase Equilibria*, 2020. **503**: p. 112316.
- 361
- 362 27. Bonhote, P., et al., *Hydrophobic, highly conductive ambient-temperature molten salts*.  
363 *Inorganic chemistry*, 1996. **35**(5): p. 1168-1178.
- 364
- 365 28. Yakdi, N.E., et al., *Detection and sizing of single droplets flowing in a lab-on-a-chip*  
366 *device by measuring impedance fluctuations*. *Sensors and Actuators B: Chemical*, 2016.  
367 **236**: p. 794-804.



368  
369  
370  
371  
372  
373  
374  
375  
376  
377  
378  
379  
380  
381  
382  
383  
384  
385

29. Mabbott, G.A., *An introduction to cyclic voltammetry*, Journal of Chemical Education, 1983, **60**(9): p. 697-702.
30. Wasserscheid, P. and T. Welton, *Ionic liquids in synthesis*. 2008: John Wiley & Sons.
31. Ghimire, P. C, et al., *In-situ tools used in vanadium redox flow battery research - Review*. Batteries, 2021, **7**(3) 53.
32. Amatore, C., et al., *Theory and experiments of transport at channel microband electrodes under laminar flows. 2. Electrochemical regimes at double microband assemblies under steady state*. Analytical chemistry, 2008. **80**(24): p. 9483-9490.
33. Amatore, C., et al., *Theory and experiments of transport at channel microband electrodes under laminar flows. 1. Steady-state regimes at a single electrode*. Analytical chemistry, 2007. **79**(22): p. 8502-8510.

## Table and Figure captions

386  
387  
388  
389  
390  
391  
392  
393  
394  
395  
396  
397  
398  
399  
400  
401  
402  
403  
404  
405  
406  
407  
408  
409  
410  
411

**Table 1** Chemical structures and aspect of the compounds used for the preparation of electrolytes.

**Table 2** Influence of the flow rate ratio on the laminar flow and the open circuit potential.

**Fig. 1** Schematic design of the microfluidic cell.

**Fig. 2** (a) CVs performed with an Au electrode (200  $\mu\text{m}$  in diameter) in a 0.1 M  $\text{FeCl}_2$  in  $\text{C}_2\text{mimTFSI}$  at different scan rates, the black line corresponds to the electrochemical window, (b) variation of the anodic peak current as a function of  $\sqrt{v}$ .

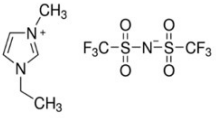
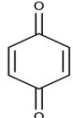




**Fig. 3** (a) CVs performed with an Au electrode (200  $\mu\text{m}$  in diameter) in a 0.35 M Quinone in  $\text{C}_2\text{mimTFSI}$  at different scan rates, the black line corresponds to the electrochemical window, (b) variation of the anodic peak current as a function of  $\sqrt{v}$ .

**Fig. 4** CVs performed with a gold electrode (200  $\mu\text{m}$  in diameter) in a 0.1 M  $\text{FeCl}_2$  (blue curve) in a 0.35 M Quinone (black curve) in  $\text{C}_2\text{mimTFSI}$  at  $200 \text{ mVs}^{-1}$ .

**Fig. 5** Variations of the viscosity of pure  $\text{C}_2\text{mimTFSI}$ , solution of 0.35 M quinone in  $\text{C}_2\text{mimTFSI}$  and solution of 0.1 M  $\text{FeCl}_2$  in  $\text{C}_2\text{mimTFSI}$  as a function of temperature.

**Fig. 6** (a) Experimental set-up and polarization curves of the cell for total flow rate of (b) 10  $\mu\text{L}\cdot\text{min}^{-1}$  and (c) 20  $\mu\text{L}\cdot\text{min}^{-1}$ .

412 **Table 1** Chemical structures and aspect of the compounds used for the preparation of  
 413 electrolytes.



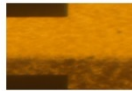
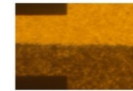
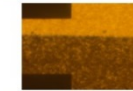
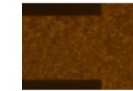
Electrolyte	C <sub>2</sub> mimTFSI	Quinone (0.35 M) in C <sub>2</sub> mimTFSI	FeCl <sub>2</sub> (0.1 M) in C <sub>2</sub> mimTFSI
Chemical structure			
Aspect			

414

415

416 **Table 2** Influence of the flow rate ratio on the laminar flow and the open circuit potential.

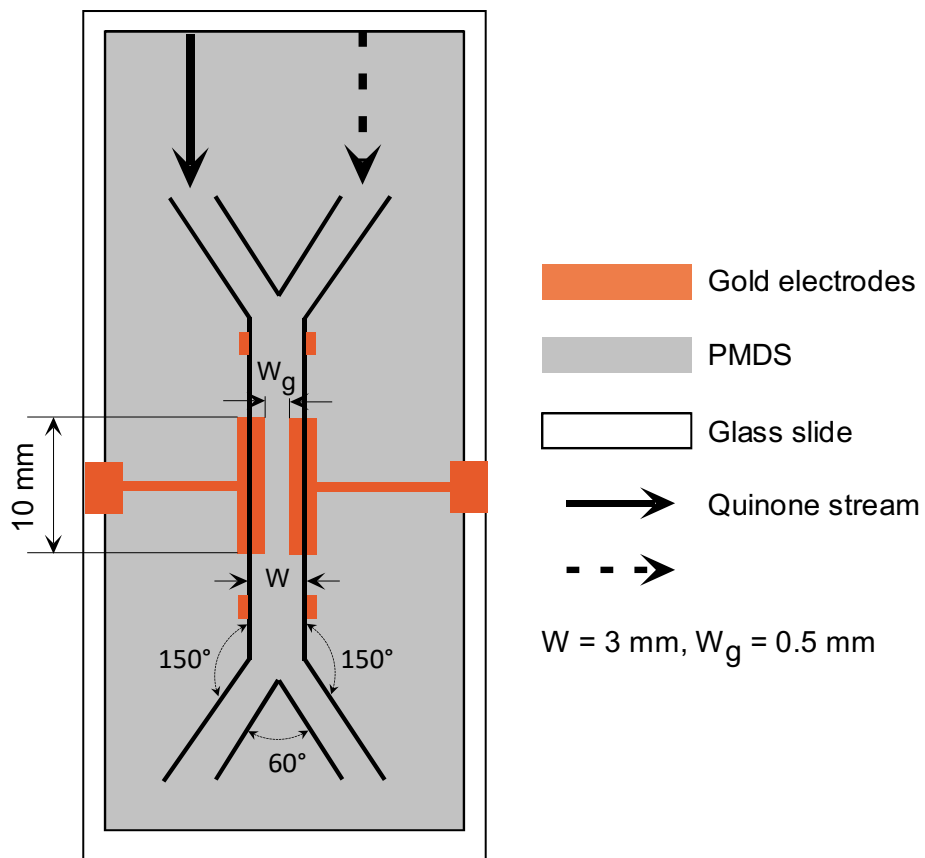
417

Flow-rate ( $\mu\text{l. min}^{-1}$ )	0 – 30	5 – 25	10 – 20	15 – 15	20 – 10	30 – 0
Images						
$E_{oc}$ (V)	0	0.48	0.52	0.61	0.61	0

418

419

420



421

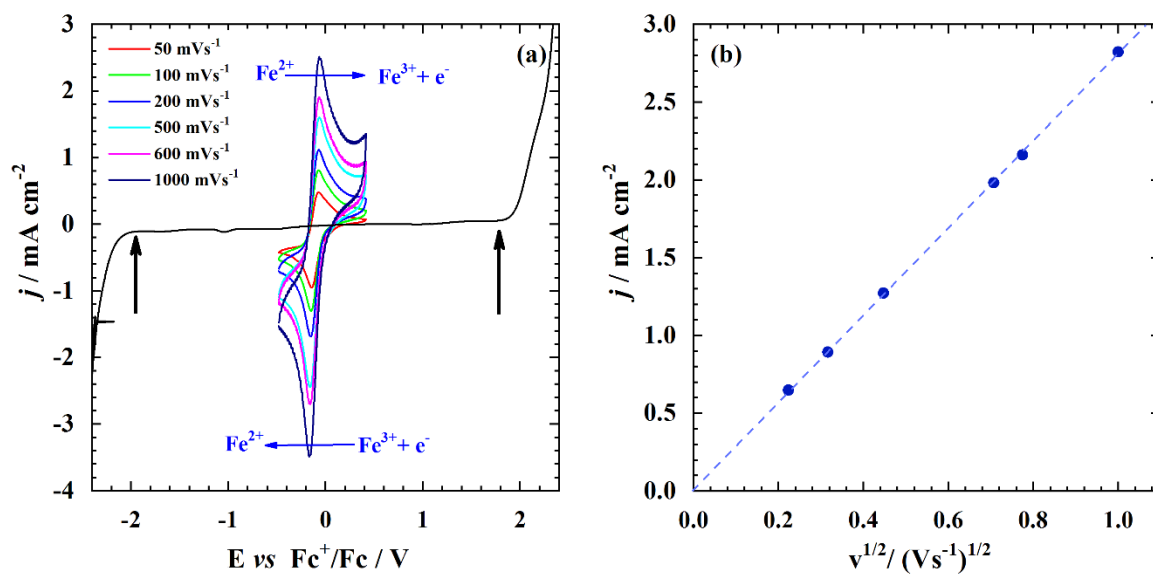
422

423 **Fig. 1** Schematic design of the microfluidic cell.

424

425

426



427

428

429 **Fig.2** (a) CVs performed with an Au electrode (200  $\mu\text{m}$  in diameter) in a 0.1 M FeCl<sub>2</sub> in

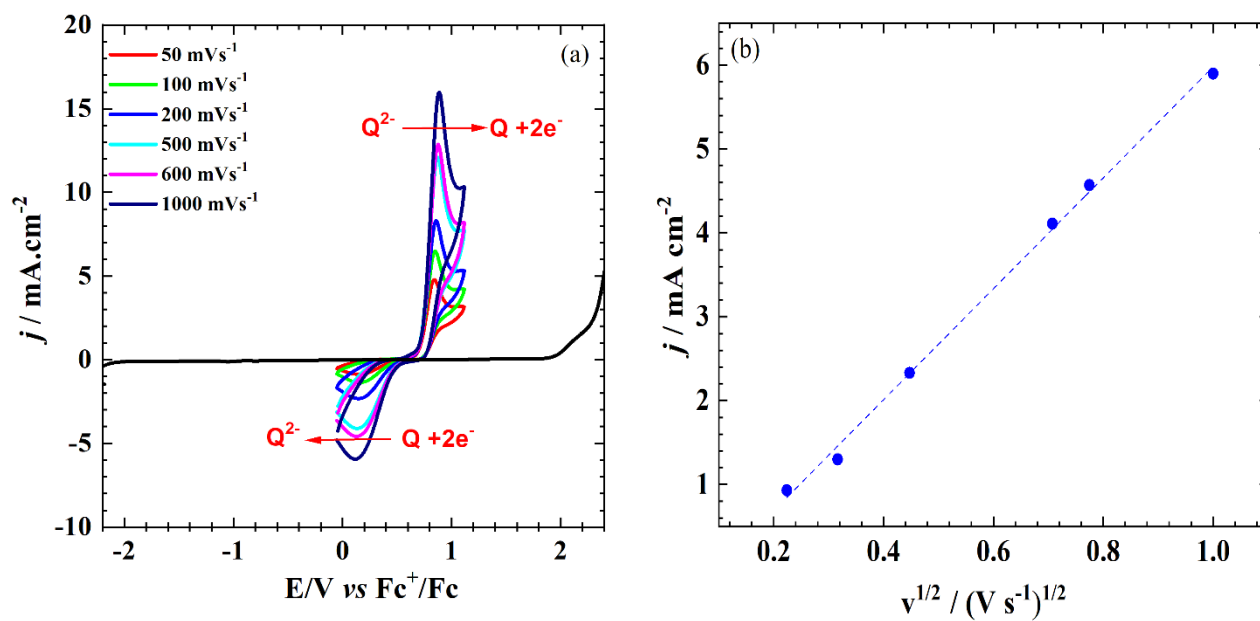
430 C<sub>2</sub>mimTFSI at different scan rates, the black line corresponds to the electrochemical

431 window, (b) variation of the anodic peak current as a function of  $\sqrt{v}$ .

432

433

434



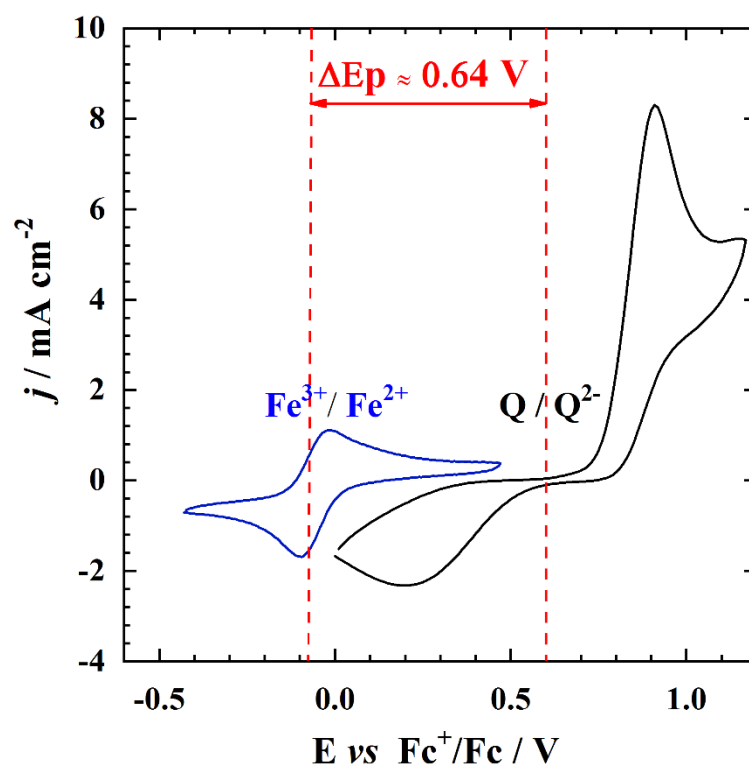
435

436

437 **Fig. 3** (a) CVs performed with an Au electrode (200  $\mu$ m in diameter) in a 0.35 M Quinone in  
 438  $C_2mimTFSI$  at different scan rates, the black line corresponds to the electrochemical  
 439 window, (b) variation of the anodic peak current as a function of  $\sqrt{v}$ .

440

441



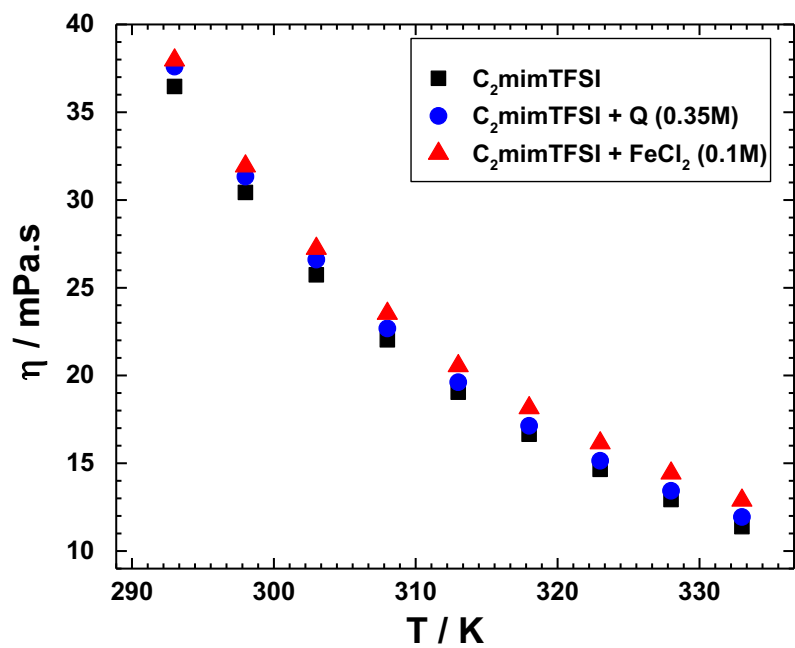
442

443

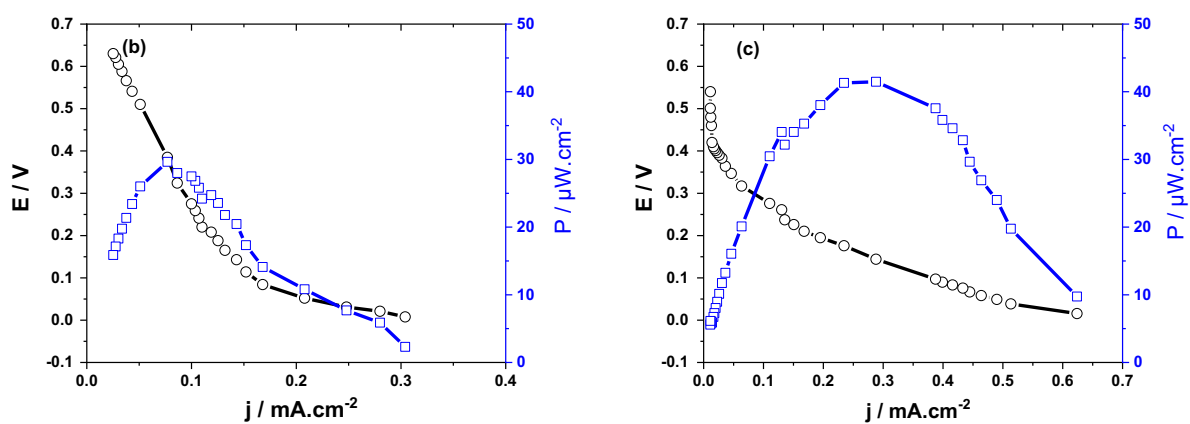
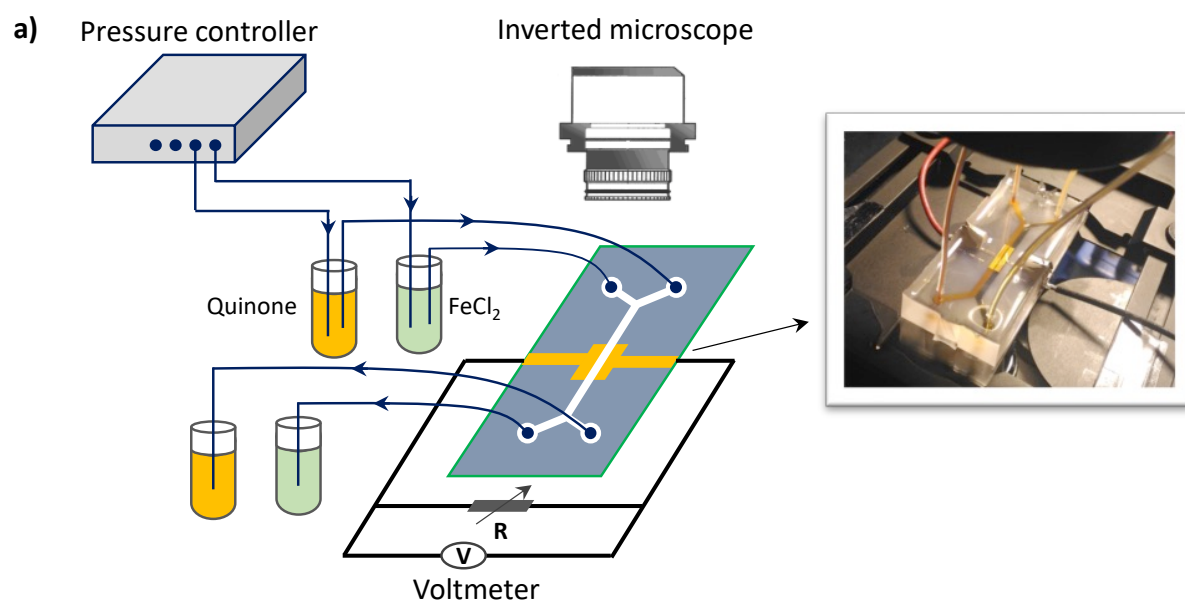
444 **Fig. 4** CVs performed with a gold electrode (200  $\mu\text{m}$  in diameter) in a 0.1 M  $\text{FeCl}_2$  (blue curve)  
445 in a 0.35 M Quinone (black curve) in  $\text{C}_2\text{mimTFSI}$  at  $200 \text{ mVs}^{-1}$ .

446





447  
 448 **Fig.5** Variations of the viscosity of pure C<sub>2</sub>mimTFSI, solution of 0.35 M quinone in  
 449 C<sub>2</sub>mimTFSI and solution of 0.1 M FeCl<sub>2</sub> in C<sub>2</sub>mimTFSI as a function of temperature.  
 450



452

453 **Fig. 6** (a) Experimental set-up and polarization curves of the cell for total flow rate of (b) 10  
 454  $\mu L \cdot min^{-1}$  and (c) 20  $\mu L \cdot min^{-1}$ .

455